



# Modelling and corrosion of coated stainless steel substrates for bipolar plates at different temperatures

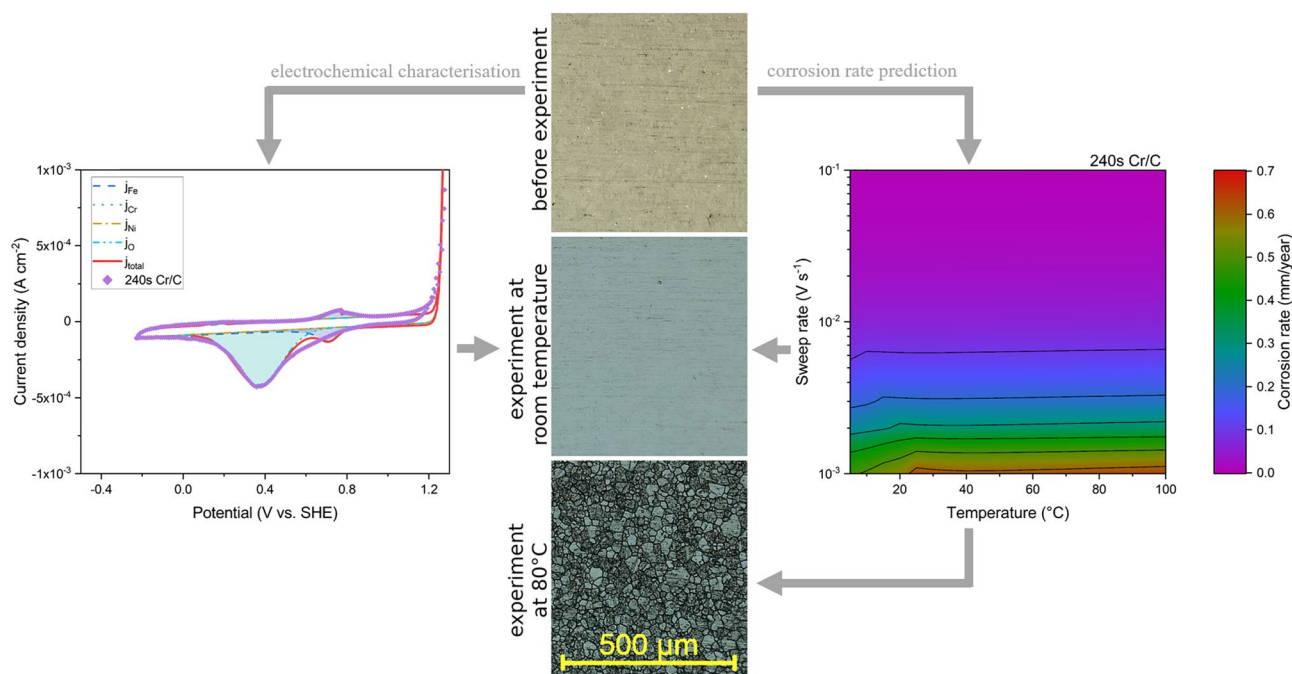
Maximilian Steinhorst<sup>1,2</sup> · Michael Auinger<sup>3,4</sup> · Teja Roch<sup>1</sup> · Christoph Leyens<sup>1,2</sup>

Received: 16 August 2022 / Accepted: 22 January 2023  
© The Author(s) 2023

## Abstract

The corrosion behaviour of coated stainless steel as bipolar plate material in PEM fuel cell applications and its improvement through the surface modifications was investigated. A commercial SS316L stainless steel grade was deposited with thin multi-layer coatings, consisting of a carbon top layer and a chromium interlayer of two different thicknesses. Interfacial contact resistance measurements revealed that the applied Cr/C coatings are highly conductive and surpass the ICR criteria, suggested by the U.S. Department of Energy. Corrosion resistance was thoroughly analysed by potentiodynamic polarisation and cyclic voltammetry in 0.5 M H<sub>2</sub>SO<sub>4</sub> at room temperature and 80 °C, respectively, combined with numerical modelling. Electrochemical results agree well with numerical modelling, including the dissolution of metallic species, local pH-shifts and changes of electrolyte conductivity. Furthermore, the study shows that the application of a Cr/C coating significantly reduces the current density in the passive region during potentiodynamic polarisation and lowering the corrosion rate of the steel substrate by at least a factor of two.

## Graphical abstract



**Keywords** Bipolar plate · Corrosion · Interfacial contact resistance · Modelling · Thin films

Extended author information available on the last page of the article

## 1 Introduction

In view of the current situation, which indicates that the global energy consumption remains high, the development of efficient and eco-friendly technologies is imperative [1]. It is projected that the energy consumption will increase even further in specific areas [2, 3]. In this context, fuel cells are a promising and versatile option [4]. Especially the polymer electrolyte membrane fuel cell (PEMFC) is a key technology towards a climate-friendly mobility due to its low emissions, good efficiency and high user convenience, including long travel distances and fast refuelling cycles [5]. There are high requirements for the bipolar plate (BPP) of a PEMFC such as good mechanical stability, high corrosion resistance and good electrical as well as thermal conductivity. Among the different BPP materials, stainless steel exhibits a promising combination of properties [6–9]. However, the native oxide reduces the electrical contact to the adjacent gas-diffusion layer (GDL) and the steel corrodes in the harsh PEMFC operating conditions [10, 11]. A low interfacial contact resistance (ICR) between the BPP and GDL is mandatory because the ICR contributes to a great extent to the ohmic resistance in a fuel cell. By this, the ICR plays a major role in the performance losses and has a significant impact on the efficiency [12–14]. Moreover, the loss of cell voltage as a consequence of corrosion has been identified as a significant problem that reduces the longevity of PEMFCs [15]. To prevent corrosion and at the same time increase the electrical conductivity, a wide range of BPP surface modifications were investigated. These modifications range from pure metallic and various metallic compounds [10, 16–21] to different carbon-based thin films [22–29]. Hereby, carbon-based coatings show excellent results rendering them a promising coating material for fuel cell applications [30].

Miyazawa et al. [31] studied the corrosion of bare stainless steel substrates as anode material. They reported that the main reason for the performance decline was the increase of contact resistance during the experiments. The degradation of a carbon-coated stainless steel bipolar plate has further been studied by Papadiaz et al. [32] and a numerical point-defect model for the increase of the contact resistance has been proposed. All of the aforementioned studies were carried out at a single temperature and without the application of a metallic interlayer between the substrate and carbon coating. Numerous investigations on the corrosion mechanisms and the effect of alloy elements such as molybdenum to increase pitting resistance have been reported [33–35].

In this study, we investigate the corrosion processes of PVD-coated 316 L stainless steel (SS316L) samples

under conditions comparable to the PEMFC environment using a combination of electrochemical experiments and an adapted thermochemical model. By this approach, the main reactions can be modelled to derive the individual impact on the overall process and eventually to identify the governing mechanism for corrosion. A total of four different coatings were deposited onto SS316L substrates to examine the influence on the corrosion properties. Hereby, two single metallic thin films with different thicknesses and two multi-layer coatings containing the metallic thin films as interlayer and the same carbon top layer were prepared. Results were compared to a comprehensive thermochemical model to examine the influence of the scan rate and temperature on the corrosion rate of the substrate material and multi-layer coating.

## 2 Experimental/modelling methods

### 2.1 Materials

Austenitic stainless steel (SS316L) substrates of 0.1 mm thickness were cleaned with distilled water, methanol and dried with nitrogen before putting them on holders for the vacuum deposition. The chemical composition is listed in Table 1.

A cathodic arc deposition system was employed for depositing the chromium and carbon-based coatings. The vacuum chamber was evacuated to a base pressure between  $10^{-3}$  and  $10^{-4}$  Pa using a rotary and a turbo molecular pump. In order to remove the native oxide layer from the substrates, an ion sputtering process was conducted. The chamber was then heated up to 300 °C and the operating pressure was set to approximately  $10^{-1}$  Pa. Onto the cleaned SS316L substrates, chromium was deposited from a pure chromium target (99.8 %) using two different deposition times, 120 s and 240 s, respectively. Additionally, a carbon layer from a 99.99 % graphite target was applied on some samples. The average thickness values, measured by X-ray reflectivity, of the deposited thin films are listed in Table 2.

**Table 1** Chemical composition of commercial austenitic stainless steel 316 L, used in this study

C (wt%)	Mn (wt%)	Cr (wt%)	Ni (wt%)	Mo (wt%)	Fe (wt%)
0.02	1.34	17.03	10.95	2.02	Bal.

The composition matches the nominal concentration ranges for this industrial grade [36]

**Table 2** Measured thickness values of the Cr-coated and Cr/C-coated samples

Sample name	Interlayer	Top layer	Thickness (nm)
120 s Cr	–	Cr	18
240 s Cr	–	Cr	27
120 s Cr/C	Cr	C	66
240 s Cr/C	Cr	C	75

The substrate was stainless steel SS316L in all cases

## 2.2 Interfacial Contact Resistance

In this work, the determination of the interfacial contact resistance (ICR) follows the procedures described by Davies et al. [6] and Wang et al. [7]. Hence, the ICR is determined by varying the compaction force, ranging from 25 to 200 N cm<sup>-2</sup>. For the measurement setup, a tensile tester for applying the compaction force and an electrical circuit attached to two gold-coated copper blocks were used. The sample is placed between two sheets of GDL and the potential drop  $V$  is measured by an ohmmeter with a set measuring current  $I$ . Considering the (measurement) surface area  $A_s$ , the total resistance  $R_{\text{total}}$  can be calculated via

$$R_{\text{total}} = V I A_s. \quad (1)$$

By measuring the ICR of one GDL sheet, the individual contact resistance of the sample can be determined.

## 2.3 Electrochemical characterisation

The corrosion behaviour was studied by potentiodynamic polarization and cyclic voltammetry (CV) tests in 0.5 M H<sub>2</sub>SO<sub>4</sub> solution at room temperature and 80 °C, which corresponds to the typical operating conditions of a PEMFC [4, 5]. The measurement setup consists of a Metrohm Autolab PGSTAT302N potentiostat/galvanostat and an electrochemical cell with a three-electrode setup including the sample as working electrode, a platinum rod as counter electrode and a saturated Ag/AgCl reference electrode. Prior the potentiodynamic tests, the open circuit potential (OCP) was measured for 1 h. The potentiodynamic polarization measurements were performed between  $-0.5$  and  $1.5$  V vs. standard hydrogen electrode (SHE) at a scan rate of  $0.001$  V s<sup>-1</sup>.

CV was used to evaluate the reduction and oxidation reactions of the different specimens in the described simulated PEM fuel cell conditions. The measurements were conducted with the same experimental setup as for potentiodynamic polarization tests. In total, three cycles between  $\pm 1$  V vs. OCP, with a constant sweep rate of  $0.01$  V s<sup>-1</sup>,

were performed. For the analysis, only the third cycle of the measurement was taken into account. The zero current potentials of the negative and positive sweep of the third CV scan have been averaged in order to remove the hysteresis effect due to capacitive losses [37]. This averaged value is used for the thermochemical modelling.

## 2.4 Modelling

The mathematical model for simulating the CV experiments and deriving the corrosion rates is based on a bottom-up approach, using the commercial software package MATLAB 2022 (Mathworks Inc.). Therefore, the microscopic current contributions of surface pH-value shifts  $j_{\text{pH-shift}}$  [38], material corrosion  $j_{\text{corrosion}}$  [37] as well as the ohmic resistance of the solution  $j_{\text{solution}}$  [37] and further ohmic resistances due to formed oxide layers and contact resistances of the equipment  $j_{\text{contact}}$  were calculated individually. These were eventually combined to a macroscopic current flow, representing the total current density  $j_{\text{total}}$  as expressed by Eq. (2)

$$j_{\text{total}} = j_{\text{pH-shift}} + j_{\text{corrosion}} + j_{\text{solution}} + j_{\text{contact}}. \quad (2)$$

The current contribution due to the pH-shift, shown in Eq. (3), originates from the pH-gradient across the width of the diffusion zone  $\delta_{\text{eff}}$  between the surface of the electrode and the bulk solution

$$j_{\text{pH-shift}} = \frac{F}{\delta_{\text{eff}}} \left[ D_{\text{H}^+} (c_{\text{H}^+}^{\text{surface}} - c_{\text{H}^+}^{\text{solution}}) - D_{\text{OH}^-} K_w \left( \frac{1}{c_{\text{H}^+}^{\text{surface}}} - \frac{1}{c_{\text{H}^+}^{\text{solution}}} \right) \right], \quad (3)$$

where  $F$  is the Faraday constant ( $F = 96485$  A s mol<sup>-1</sup>),  $c_i^x$  the concentration of species  $i$  at position  $x$  and  $D_i$  the diffusion coefficient of species  $i$ .  $K_w$  is the autoprotolysis equilibrium of water at given temperature.

This pH-shift is a general effect occurring in all aqueous electrochemical reactions and was calculated from an analytical solution of the CV-signal in an unbuffered electrolyte, published in earlier works [38]. The diffusion of hydronium (H<sub>3</sub>O<sup>+</sup>) and hydroxide (OH<sup>-</sup>) species was considered not to be altered by the formation of iron, chromium and nickel (oxy-)hydroxides which may form near the electrode surface at very low potentials.

Because the kinetics of the hydrogen oxidation/evolution reactions (HOR/HER) are faster than the diffusion of dissolved hydrogen to and from the electrode surface [39–41], the computed current density in Eq. (3) may become unreasonably high and diffusion limitation by depletion of dissolved hydrogen in the electrolyte needs to be considered. This could be solved numerically by including the Butler–Volmer kinetics as flux condition for the boundary

condition at the electrode surface. However, because an analytical solution cannot be derived for the general case, it is assumed that the hydrogen diffusion will not be obstructed by the transport of hydronium or hydroxide species. With this assumption, which is in good agreement with thermodynamic expectations [37], the flux of hydrogen towards the electrode can be calculated by the concentration gradient between electrode surface and bulk solution

$$j_{\text{pH-shift}} = 2FD_{\text{H}_2} \frac{c_{\text{H}_2}^{\text{surface}} - c_{\text{H}_2}^{\text{solution}}}{\delta_{\text{eff}}} \quad (4)$$

From Eq. (4), the diffusion-limiting current can be calculated by setting the concentration of dissolved hydrogen at the electrode surface to zero [37]. Depending on the actual hydrogen partial pressure at the electrode surface, one needs to interpolate the corresponding pH-value from Eq. (3) for a given current density and to compensate the shift in the electrochemical potential  $E$  with the hydrogen partial pressure ( $p_{\text{H}_2}$ ) term from the Nernst equation (Eq. 5)

$$E = E^0 + \frac{RT}{zF} \ln \left( \frac{a_{\text{ox}}}{a_{\text{red}}} \right) \approx -58 \text{ mV} \cdot \text{pH} - 29 \text{ mV} \cdot \log_{10} p_{\text{H}_2}, \quad (5)$$

where  $R$  is the universal gas constant ( $R = 8.3144 \text{ J mol}^{-1} \text{ K}^{-1}$ ) and  $T$  the absolute temperature. The corrosion of chromium, nickel and iron was calculated numerically from the diffusion of the corresponding ionic species  $\text{Fe}^{2+}$ ,  $\text{Fe}^{3+}$ ,  $\text{Cr}^{2+}$ ,  $\text{Cr}^{3+}$ ,  $\text{CrO}_4^{2-}$ ,  $\text{Ni}^{2+}$  in the electrolyte (Eq. 6) assuming dissolution from the electrode surface according to Butler-Volmer kinetics (Eq. 7). The exchange current density  $j_0$  for all metals was fitted to experimental data from the corrosion tests as well as compared to typical values from literature [37, 39, 42]. The species  $\text{Ni}^{4+}$  was not considered in the simulation, because the acid redox equilibrium  $\text{NiO}_2 + 2\text{H}^+ + 2\text{e}^- \rightleftharpoons \text{Ni}^{2+} + 2\text{OH}^-$  has an  $E^0$  of 1.59 V, which is higher than the dissociation potential of water ( $E^0 = 1.23 \text{ V}$ )

$$\frac{\partial c_{(x,t)}}{\partial t} = \text{div}(D \cdot \nabla c_{(x,t)}), \quad (6)$$

$$\frac{\partial c_{(0,t)}}{\partial x} = \frac{j_0}{zF} \left( e^{(1-\alpha)\frac{zF}{RT}\Delta E} - e^{-\alpha\frac{zF}{RT}\Delta E} \right). \quad (7)$$

A time interval of 0.1 s was chosen to allow free diffusion with no flux conditions at the electrode surface before the change of concentration near the electrode was re-adjusted to the new potential by the Butler-Volmer equation. The spatial resolution of the numerical grid was defined by the time interval and the diffusion coefficient via  $\Delta x = 0.1\sqrt{Dt}$ . This allowed for an effective calculation of the iron/chromium

distribution and represents a good approximation for the modelled sweep rates in this study, which ranged between 1 and 100  $\text{mV s}^{-1}$ .

Ohmic resistance for the bulk solution current density was derived from the temperature-dependent molar ionic conductivities  $\lambda$  of all ionic species in the electrolyte ( $\text{H}_3\text{O}^+$ ,  $\text{OH}^-$ ,  $\text{SO}_4^{2-}$ ,  $\text{Fe}^{2+}$ ,  $\text{Fe}^{3+}$ ,  $\text{Cr}^{2+}$ ,  $\text{Cr}^{3+}$ ,  $\text{Cr}_2\text{O}_4^{2-}$ ,  $\text{Ni}^{2+}$ ), including the dissolved metal ions. In the absence of a complete and reliable dataset for the temperature-dependent specific ionic conductivities  $\kappa$ , values were derived from the combination of the Nernst-Einstein equation (Eq. 8, [37, 41]) and the Stokes-Einstein equation (Eq. 9, [41])

$$\lambda = \frac{z^2 F^2}{RT} cD, \quad (8)$$

$$D = \frac{k_B T}{6\pi\eta r}, \quad (9)$$

where  $z$  is the absolute charge value of the ionic species and  $k_B$  the Boltzmann constant ( $k_B = 1.3806 \times 10^{-23} \text{ m}^2 \text{ kg s}^{-2} \text{ K}^{-1}$ ). This links the molar ionic conductivities  $\lambda$  with temperature, the hydrodynamic radius  $r$  (i.e. the radius of the ion plus its solvation shell [41]) and the dynamic viscosity of water  $\eta$ . Assuming that the hydrodynamic radius does not change with temperature and given an empirical relation for the dynamic viscosity of water [41], one obtains the following relation for the temperature-dependent ionic conductivities. Here, the temperature  $\theta$  needs to be inserted in degrees Celsius.

$$\lambda_i = 0.889 \lambda_i^{25^\circ\text{C}} 10^{\frac{1.37023(\theta-20)+8.3610^{-4}(\theta-20)^2}{109+\theta}}. \quad (10)$$

The current contribution then calculates from the total potential drop and the ohmic resistance  $R_{\text{solution}}$ , calculated from the conductivity of all ionic species  $i$  ( $\text{H}_3\text{O}^+$ ,  $\text{OH}^-$ ,  $\text{SO}_4^{2-}$ ,  $\text{Fe}^{2+}$ ,  $\text{Fe}^{3+}$ ,  $\text{Cr}^{3+}$ ,  $\text{Cr}_2\text{O}_4^{2-}$ ,  $\text{Ni}^{2+}$ ) in solution [37]

$$j_{\text{solution}} = \frac{E - E_{\text{OCP}}}{R_{\text{solution}}} = (E - E_{\text{OCP}}) \frac{\kappa A}{d} = (E - E_{\text{OCP}}) \frac{A}{d} \sum_i z_i \lambda_i c_i, \quad (11)$$

where  $A$  is the electrode surface area and  $d$  the distance between electrodes. The contact resistance between the electrodes on the equipment side as well as the ohmic resistance of formed inhibition layers on the electrodes were used as fit parameters and derived from the difference to experimental values. The contribution to the current density was modelled in a similar way as shown in Eq. (11). A default value of 10  $\Omega$  was chosen for the contact resistance of the equipment. The resistance of formed oxide layers during the modelled corrosion cycles was derived from the molar amounts of dissolved chromium and iron (see Eq. 7) above

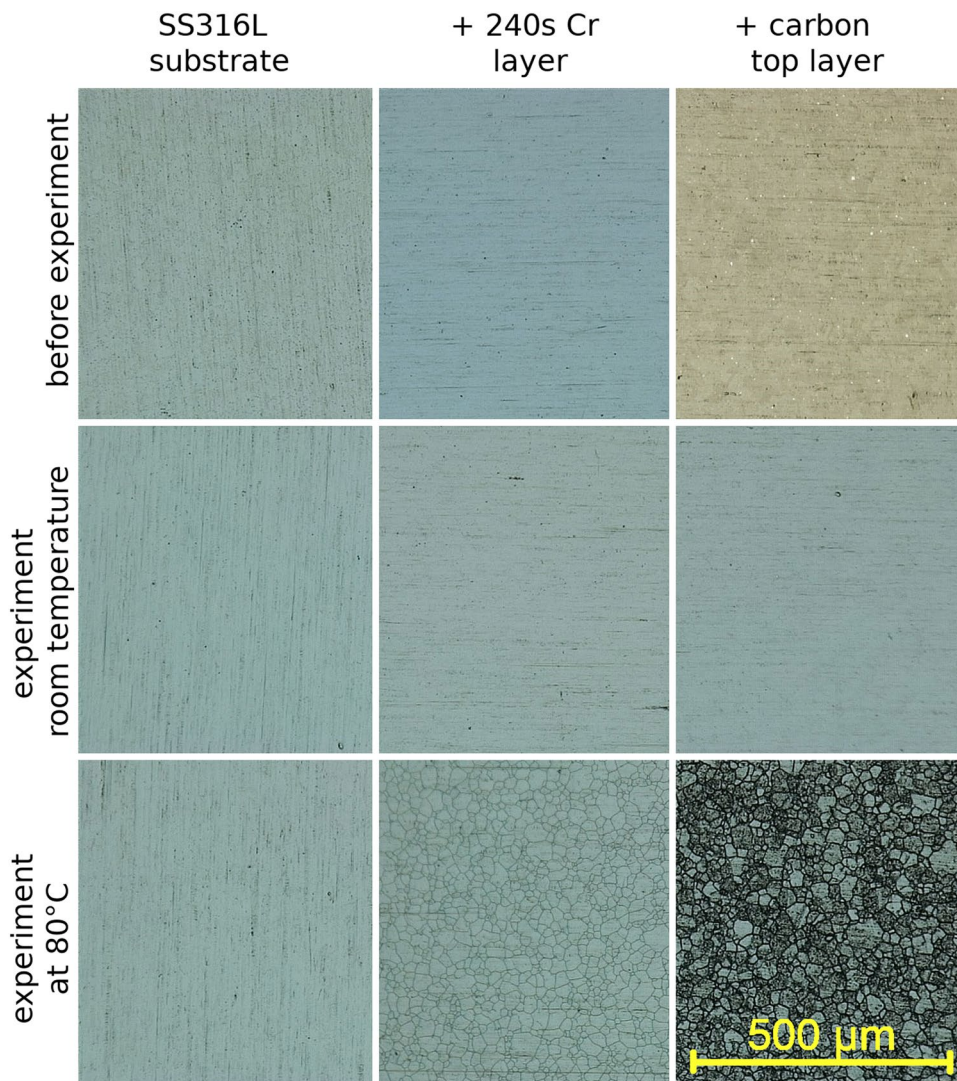


the solubility limit, the molar volumes of  $\text{Cr}_2\text{O}_3$ ,  $\text{Fe}_2\text{O}_3$ ,  $\text{NiO}$  and the specific resistances of these oxides. To compensate for the hysteresis in the CV measurements, a term for the non-Ohmic losses of the current density (capacitance/inductance) has been added, following the physical principles of loading and unloading a capacitor [37]. Since the origin of the non-Ohmic losses has not been investigated in detail in this study, the time constant  $\tau (= RC)$  (see Eq. 12) has been treated as a pure fit parameter and was varied between all approximations

$$j_{\text{non-ohmic}} = j_{\text{max}} \left( 1 - e^{-\frac{t}{\tau}} \right). \quad (12)$$

Graphical output of obtained modelling results is shown in the style of a cyclic voltammogram where the total current density has been normalised to an electrode surface area of  $1 \text{ cm}^2$ . The influence of temperature and potential sweep rates is displayed in the form of 2-dimensional contour plots of the corrosion rate.

**Fig. 1** Light microscopy images of the surface of stainless steel (SS316L), SS316L with 240 s Cr deposited and SS316L with 240 s Cr deposited and a carbon top layer before (top) and after cyclic voltammetry tests in  $0.5 \text{ M H}_2\text{SO}_4$  at room temperature (middle) and  $80^\circ\text{C}$  (bottom)



### 3 Results and discussion

The visual appearance of the samples before and after the CV measurements revealed a homogeneous surface, as shown in Fig. 1. This is also a good indication that the thickness of the deposited coating layers is homogeneous. The measured specimens at room temperature exhibit no apparent changes except for the carbon-coated sample. In contrast to that, the corrosion at  $80^\circ\text{C}$  appears to be more significant. Here, the surface of the coated samples showed clear differences between grains and grain boundaries which might be caused by specific grain boundary attack of the acid during corrosion.

#### 3.1 Interfacial contact resistance

Figure 2 displays the interfacial contact resistance as a function of the applied compaction force for (a) the uncoated

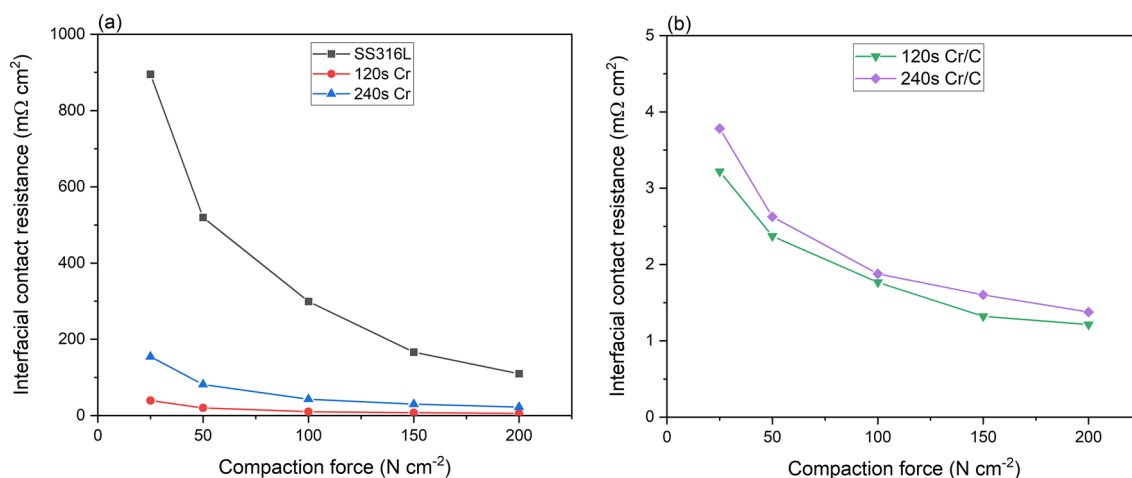


**Fig. 2** Interfacial contact resistance of **a** the bare SS316L, the Cr-coated and **b** Cr/C-coated samples depending on the applied compaction force

stainless steel substrate and (b) the coated samples. In general, it can be seen that the ICR drops quickly up to a compaction force of  $100 \text{ N cm}^{-2}$  due to the constantly increasing area between the sample and the GDL. The uncoated SS316L has significantly higher ICR values in the entire measurement range. Both Cr coatings already reduce the resistance by more than 75 %. A clear difference between the chromium-coated samples can be seen, and the 240 s Cr coating has higher ICR values compared to the 120 s Cr coating. This can be attributed to a thicker native oxide layer. However, both coatings do not meet the required threshold in the DOE 2020 criteria of  $10 \text{ m}\Omega \text{ cm}^2$  [43], even at a the applied maximum of  $250 \text{ N cm}^{-2}$ . The carbon-based coatings greatly lower the contact resistance of the substrate and ICR values are below  $2 \text{ m}\Omega \text{ cm}^2$  at  $150 \text{ N cm}^{-2}$ .

### 3.2 Potentiodynamic polarization

The uncoated SS316L substrate exhibits the highest corrosion current density  $j_{\text{corr}}$  of all samples, approximately  $1.8 \times 10^{-5} \text{ A cm}^{-2}$  and the lowest polarization resistance  $R_p$ , which corresponds to the oxidation resistance of a material during an applied (external) voltage [37]. Figure 3a depicts the electrochemical polarization curves of all specimens at

room temperature in  $0.5 \text{ M H}_2\text{SO}_4$ , and the corresponding corrosion parameters are listed in Table 3.

After reaching the corrosion potential  $E_{\text{corr}}$ , the stainless steel remains inert in the corrosive environment and the formation of a protective oxide layer starts around  $0 \text{ V}$ , which is characterised by the strong oxidation peak. The critical anodic current density is approximately  $1.7 \times 10^{-4} \text{ A cm}^{-2}$  at this potential. Between  $1.1$  and  $1.2 \text{ V}$ , the bare steel enters the transpassive state, which is the potential range for the transpassive reaction of chromium [44] and can be observed from the steep increase in current density. The dissociation of the electrolyte, i.e. water, via  $2\text{H}_2\text{O} \rightleftharpoons \text{O}_2 + 4\text{H}^+ + 4\text{e}^-$  occurs in a similar potential range ( $E^0 = 1.23 \text{ V}$ ), additionally leading to the rise of the current density.

The deposited chromium thin films, i.e. 120 s Cr and 240 s Cr, slightly improve the corrosion resistance of the stainless steel, which can be seen in the higher polarization resistances of  $876$  and  $1995 \Omega \text{ cm}^2$ , respectively (see Table 3). This is because of the high chromium content in the base material ( $\approx 17 \text{ wt}\% \text{ Cr}$ ). The thin Cr coating leads to a faster formation of an oxide layer at the surface which can be concluded from the steeper decrease and generally lower anodic current density of  $1.81 \times 10^{-5} \text{ A cm}^{-2}$  before reaching the passive region. This is in agreement with the

**Table 3** Corrosion parameters of bare SS316L, the Cr-coated and Cr/C-coated samples at room temperature and  $80 \text{ }^\circ\text{C}$  in  $0.5 \text{ M H}_2\text{SO}_4$  bubbled with argon

Sample	RT			$80 \text{ }^\circ\text{C}$		
	$E_{\text{corr}}$ (V)	$j_{\text{corr}}$ ( $\text{A cm}^{-2}$ )	$R_p$ ( $\Omega \text{ cm}^2$ )	$E_{\text{corr}}$ (V)	$j_{\text{corr}}$ ( $\text{A cm}^{-2}$ )	$R_p$ ( $\Omega \text{ cm}^2$ )
SS316L	-0.118	$1.76 \times 10^{-5}$	769	-0.039	$1.55 \times 10^{-4}$	170
120 s Cr	-0.045	$6.64 \times 10^{-5}$	876	-0.049	$1.53 \times 10^{-4}$	232
240 s Cr	-0.034	$5.36 \times 10^{-6}$	1996	-0.048	$5.82 \times 10^{-5}$	210
120 s Cr/C	-0.041	$1.26 \times 10^{-6}$	25,672	-0.047	$4.91 \times 10^{-5}$	604
240 s Cr/C	-0.088	$8.22 \times 10^{-8}$	186,030	-0.054	$6.77 \times 10^{-6}$	2208

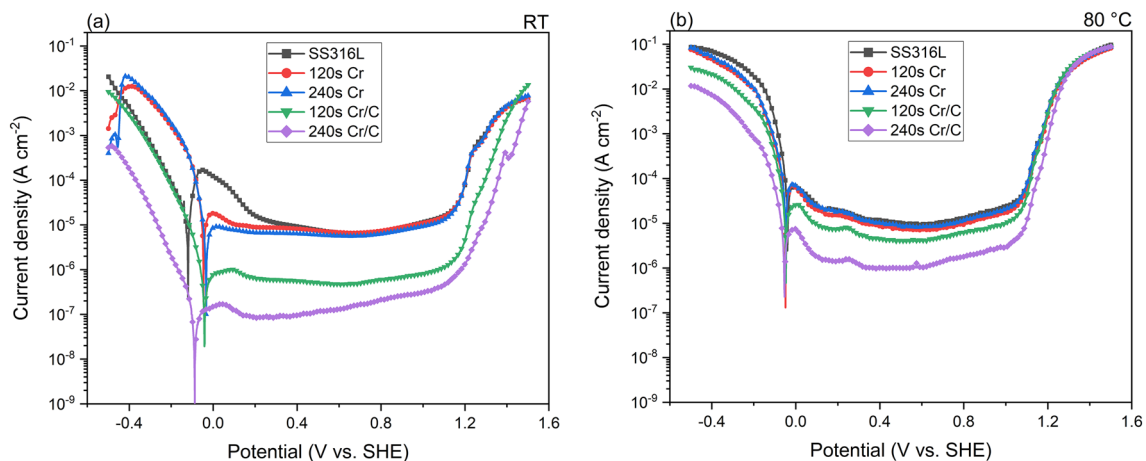


**Fig. 3** Potentiodynamic polarization curves of **a** the bare SS316L, the Cr-coated and Cr/C-coated samples in 0.5 M H<sub>2</sub>SO<sub>4</sub> bubbled with argon at room temperature and **b** at 80 °C

findings of Quang et al. [45] who investigated the tendency of stainless steel to passivate, depending on their chromium content. Moreover, Bellezze et al. [46] reported that increasing amounts of chromium are responsible for a decrease of critical anodic current densities. Consequently, the Cr layer, deposited for 240 s, leads to a further reduction of the corrosion rate, which can be attributed to the thicker film. Comparable to the uncoated SS316L substrate, both Cr coatings show a transpassive behaviour between 1.1 and 1.2 V, where the transpassive reaction of Cr starts leading to the rise in the current density [44]. At the upper operating temperature of a PEMFC, the differences between the polarization curves are less distinct, especially for the Cr-coated samples and the bare substrate (see Fig. 3b). Due to the elevated temperature, significantly higher corrosion currents  $j_{\text{corr}}$  and lower polarization resistances can be observed (see Table 3).

The carbon top layer leads to smaller corrosion currents of  $1.26 \times 10^{-6}$  A cm<sup>-2</sup> for 120 s Cr/C and  $8.22 \times 10^{-8}$  A cm<sup>-2</sup> for 240 s Cr/C samples, respectively. Moreover,  $R_p$  is increased by a factor of approximately 240 for the thicker Cr/C coating. This improvement is likely due to fewer exposed defects in the multi-layer coating. Condga et al. [25] reported that by applying a multi-layer coating, there are fewer pathways to the underlying substrate which would otherwise accelerate corrosion. It is known that PVD coatings often exhibit microstructural defects such as pores which can act as channel to the substrate for aggressive/corrosive media, i.e. acidic electrolyte [47]. In the Cr/C multi-layer coating, these pathways are covered or blocked by the carbon top layer, thus the corrosion resistance of the Cr/C coating is significantly improved. In addition to this, the improved corrosion resistance may further be improved by the thickness effect. The current density in the passive region reaches an absolute minimum amongst all samples, and therefore, less oxidation occurs in that potential range.

However, a steep increase of the current signal again occurs at the same potential as for all specimens, which is caused by water dissociation as well as the transpassive reaction of the Cr interlayer. For an electrolyte temperature of 80 °C, the plateau current for both carbon-coated samples rises by approximately two orders of magnitude, which is still one order of magnitude lower, compared to the rise of current density for the SS316L and chromium-coated specimens.

### 3.3 Cyclic voltammetry

CV measurements were used to further analyse the corrosion behaviour in the simulated PEMFC environment at room temperature and 80 °C. In Fig. 4, the CV curves of the SS316L substrate and the samples with 120 s Cr are shown. The bare substrate has a large reduction peak below -0.3 V, attributed to the reduction of dissolved oxygen (ORR) and an onset of oxidation at 1.2 V due to water dissociation. Between -0.2 V and +0.2 V, one can observe an additional peak which can be explained by an oxidation process at the sample surface. In the presence of a coating, this specific peak gets smaller, indicating a reduction of substrate corrosion. The thin Cr layer exhibits a reduction peak similar to the stainless steel sample, but a higher oxidation peak and thus stronger buildup of a passive layer. With an additional carbon top layer, the substrate oxidation peak between -0.2 V and 0.2 V gets even smaller and the strong reduction signal from the electrolyte below -0.3 V vanishes almost completely. However, a new reduction signal around 0.4 V up to 0.5 V emerges. According to data from the electrochemical series, this signal could be caused by molybdenum ( $E^0 = 0.43$  V) from the substrate, although, given the peak size, it is more likely to be linked to the carbon top layer which promotes the reaction from oxygen to OH<sup>-</sup> via  $\text{O}_2 + 2\text{H}_2\text{O} + 4e^- \rightleftharpoons 4\text{OH}^-$  ( $E^0 = 0.40$  V).

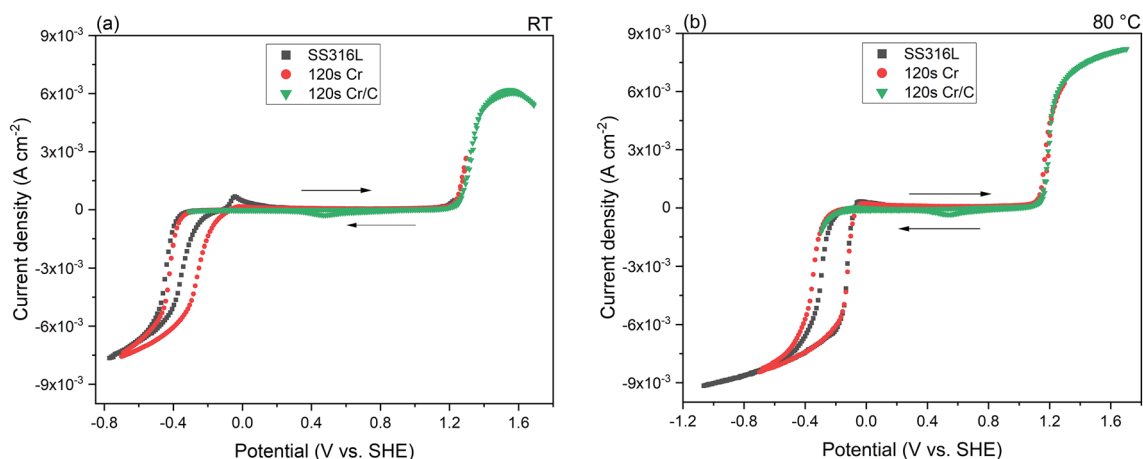


**Fig. 4** Cyclic voltammetry curves of **a** bare SS316L, 120 s Cr and 120 s Cr/C-coated samples in 0.5 M H<sub>2</sub>SO<sub>4</sub> bubbled with argon at room temperature and **b** at 80 °C. Prior to these measurements, the

OCP shift of each sample was measured for 1 h. The scan range in all cases is  $\pm 1$  V, starting from the equilibrated OCP value

Whilst an in situ analysis could not be performed during the measurement, this reduction peak was only observed for the carbon-coated samples and would correspond to the reduction of 0.110  $\mu\text{mol O}_2 \text{ cm}^{-2}$  at room temperature and at 80 °C during each cycle. The reduction of carbon would imply the presence of carbonate in the electrolyte that would have formed a voluminous precipitate, which was not observed. No signals were observed at potential values, which are typical for the alkaline nickel redox-reactions  $\text{Ni(OH)}_2 + 2e^- \rightleftharpoons \text{Ni} + 2\text{OH}^-$  ( $E^0 = -0.72$  V) and  $\text{NiO}_2 + 2\text{H}_2\text{O} + 2e^- \rightleftharpoons \text{Ni(OH)}_2 + 2\text{OH}^-$  ( $E^0 = -0.49$  V).

In accordance with the results of the polarization tests in Fig. 3, cyclic voltammetry scans of the 240 s Cr samples, which are shown in Fig. 5, exhibit smaller oxidation and reduction signals of the substrate due to the

increased thickness of the deposited chromium layer. At room temperature, the oxidation peak of the substrate is suppressed by the Cr coating, and the reduction peak of the carbon-coated sample is more pronounced. Again, this can be explained by the reduction of newly formed and adsorbed oxygen at potentials above 1.23 V, corresponding to 0.156  $\mu\text{mol O}_2 \text{ cm}^{-2}$  at room temperature and 0.060  $\mu\text{mol O}_2 \text{ cm}^{-2}$  at 80 °C.

### 3.4 Modelling

Numerical modelling of the cyclic voltammetry measurements in Sect. 3.3 has been carried out. This includes the current contributions from the pH-shift near the surface (Eq. 3), the dissolution of iron, chromium and

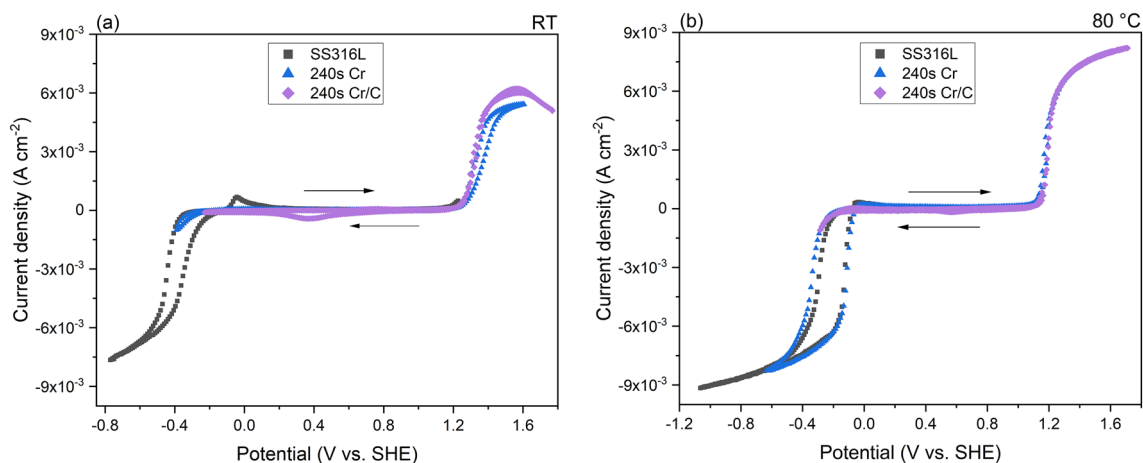


**Fig. 5** Cyclic voltammetry curves of **a** bare SS316L, 240 s Cr and 240 s Cr/C-coated samples in 0.5 M H<sub>2</sub>SO<sub>4</sub> bubbled with argon at room temperature and **b** at 80 °C. Prior to these measurements, the

OCP shift of each sample was measured for 1 h. The scan range in all cases is  $\pm 1$  V, starting from the equilibrated OCP value



nickel (Eq. 7), formation of oxides, contact resistance, the changes of electrolyte conductivity (Eq. 11) as a function of temperature and ion concentration as well as the hysteresis (Eq. 12). Especially the reactions involving chromium, nickel and iron, which lead to the anodic and cathodic peaks at intermediate potential values, are diffusion-controlled (Eq. 6). The position and size of the corrosion peaks in the experiments were fitted by varying the exchange current density  $j_0$  and charge transfer coefficient  $\alpha$  of the iron/chromium/nickel dissolution. The temperature dependency of the diffusion coefficients of all ionic species was considered via the previously mentioned procedure for the hydrodynamic radius of the ion in Eqs. 8 and 9. Water dissociation was included in the reactions via a Butler–Volmer approach (Eq. 7). Please note that the experimental data in this study show that the current density value reaches a plateau for even higher potentials. This is due to the diffusion limitation and dynamic surface coverage of the electrode with freshly formed oxygen molecules. Since the modelling approach does not include the dynamics of formation, growth and detachment of gas molecules at the electrode surface, the observed current density plateau from the experiments is hence not seen in the simulations. Including of these phenomena would require CFD simulations for gas/liquid phase mixtures which were deemed too complex and out of scope for the purpose of this study. Despite the number of input parameters for the calculations, a good agreement with experimental values could be obtained, as shown in Fig. 6.

A significant deviation of the current density for the uncoated steel sample is seen at potentials below  $-0.2$  V and can be attributed to the oxygen reduction reaction (ORR) at the sample surface [48]. Because these reactions are kinetically controlled, additional parameters would need to be

used. Instead, the modelling approach is focussed on the degradation of the electrode material. The oxidation peak near 0 V vs. SHE was attributed to the corrosion of chromium and nickel on the pure SS316L sample. This corrosion signal is biggest for the uncoated substrate and theorised to be related to the activity of both alloy elements in the steel. Whilst nickel oxides are generally poorly protective, a lower activity of chromium leads to a lower concentration of Cr ions in solution and thus slower formation of a protective chromia scale. For a chromium-coated sample, the formation of a chromia scale is expected to occur quicker, which leads to a reduction of the current peak near 0 V vs. SHE (see Fig. 5a). An applied Cr/C multi-layer would hinder the dissolution of chromium completely. Hence, the chromium plus carbon-coated sample (240 s Cr/C) exhibits a reversible signal that only corresponds to the redox equilibrium of readily dissolved iron ( $\text{Fe}^{2+}/\text{Fe}^{3+}$ ,  $E^0 = 0.77$  V). Moreover, it should be noted that the corrosion currents of the chromium-coated material are similar to values reported in literature for the uncoated specimen [44] and reduced by a factor of 10 for the Cr/C multi-layer coating (see Table 4).

After the parameters for the fitted CV curves at room temperature were obtained, the dependence of the corrosion rate with temperature and potential sweep rate was derived from the numerical model. Here, the current signal was integrated over time, following Faraday's law to obtain the total electronic charge. In order to compare between the samples in this study and link to industrially relevant corrosion rates, the total charge was converted into a corrosion rate of the matrix material (iron) where the amount of dissolved material was considered only via the hypothetical reaction  $\text{Fe} \rightleftharpoons \text{Fe}^{2+} + 2e^-$ . Together with the molar volume of iron at room temperature ( $V_m = 7.0923 \times 10^{-6}$  mol  $\text{m}^{-3}$ ),

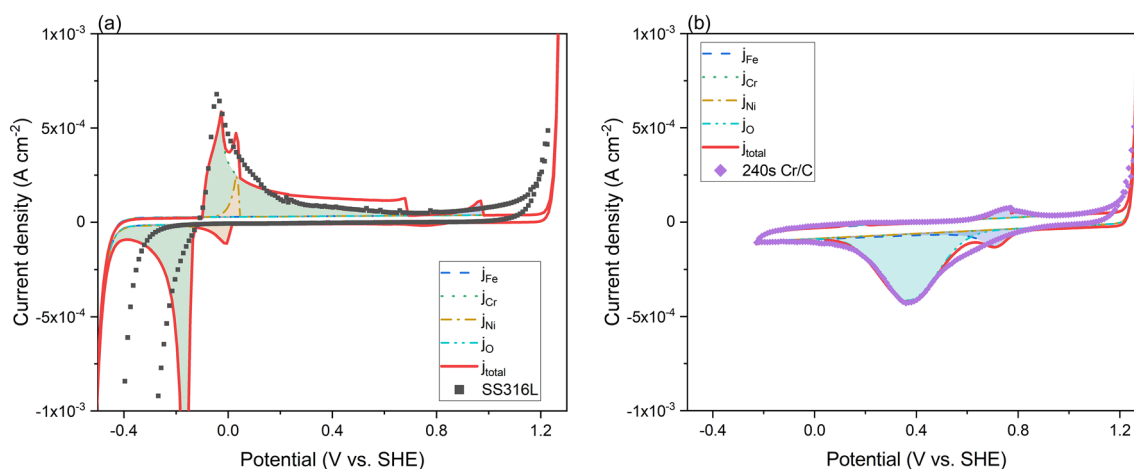


**Fig. 6** Experimental and calculated cyclic voltammetry measurements of **a** bare SS316L and **b** 240 s Cr/C-coated sample. The experimental conditions were 0.5 M  $\text{H}_2\text{SO}_4$  at room temperature. The

shaded areas underneath the peaks correspond to the current contribution from the reactions involving iron (blue), chromium (green), nickel (yellow) and carbon or oxygen (turquoise)

**Table 4** Simulation parameters for the fitted cyclic voltammetry measurements of (a) bare SS316L and (b) 240 s Cr/C-coated sample

Sample	$j_{0,\text{Fe}}$ (A cm <sup>-2</sup> )	$j_{0,\text{Cr}}$ (A cm <sup>-2</sup> )	$j_{0,\text{Ni}}$ (A cm <sup>-2</sup> )	$c_{0,\text{Fe}}^*$ (mol l <sup>-1</sup> )	$c_{0,\text{Cr}}^*$ (mol l <sup>-1</sup> )	$c_{0,\text{Ni}}^*$ (mol l <sup>-1</sup> )		
SS316L	10 <sup>-4</sup>	8.6 × 10 <sup>-5</sup>	6 × 10 <sup>-5</sup>	2.5 × 10 <sup>-5</sup>	5.0 × 10 <sup>-6</sup>	10 <sup>-6</sup>		
240 s Cr/C	10 <sup>-4</sup>	8.6 × 10 <sup>-5</sup>	0	2.5 × 10 <sup>-7</sup>	5.0 × 10 <sup>-7</sup>	10 <sup>-7</sup>		
Sample	$\alpha_{\text{Fe}}$	$\alpha_{\text{Cr}}$	$\alpha_{\text{Ni}}$	pH*	$R_{\text{contact}}$ (Ω)	$j_{\text{non-ohmic}}^{\text{max}}$ (A cm <sup>-2</sup> )	$\tau$ s <sup>-1</sup>	
SS316L	0.74	0.58	0.44	3	1	0.2	1	
240 s Cr/C	0.845	0.40	0.40	2	0.15	0.3	1.2	

The experimental conditions were 0.5 M H<sub>2</sub>SO<sub>4</sub> at room temperature. Parameters marked with an asterisk (\*) are less sensitive to the fit and may vary within a ± 10 % range

the corrosion rate was expressed as the decrease of material thickness in millimetres per year.

As can be seen in Fig. 7, the corrosion rate for the Cr/C-coated sample is much lower for all conditions in this study. This is a clear indication that the applied multi-layer coating greatly increases the corrosion resistance of the stainless steel substrate in the harsh conditions of a PEMFC. The corrosion rate tends to be larger with lower cycling rates as well as at higher temperatures. This can be explained by the fact that faster cycling means that only small amounts are dissolved per each cycle and then re-deposited again. For lower potential cycling rates, the amount of dissolved metals will be larger, thus leading to the formation of stable oxides. The higher corrosion rates observed at lower temperature in the 240 s Cr/C may be an effect of slower diffusion and the formation of higher concentrations of dissolved metal ions near the electrode surface. However, it should be stated that the temperature dependence of the standard electrochemical potential  $E_0$  as well as the solubility of formed (oxy-)hydroxides was not considered in this study due to the absence of available data. This may lead to additional deviations for the temperature dependence of the corrosion rate and will be considered for further studies.

## 4 Conclusions

Multi-layer thin films consisting of a carbon top layer plus a chromium interlayer of two different thicknesses on a commercial SS316L stainless steel substrate were analysed for their suitability as bipolar plate coating. Interfacial contact resistance was determined to evaluate the electrical conductivity. Electrochemical characterisation was conducted via potentiodynamic polarisation and cyclic voltammetry in 0.5 M H<sub>2</sub>SO<sub>4</sub> at typical operation temperatures for PEM fuel cells. Corrosion results were compared to an extensive numerical model to predict the corrosion rate as a function of temperature and potential sweep rate.

The following conclusions can be reported:

- Only small differences in the corrosion behaviour was observed between the bare SS316L substrate and the Cr thin film-coated samples, owing to the high concentrations of chromium in the substrate.
- The application of Cr/C multi-layer coating significantly reduces the resistance of the SS316L substrate, with ICR values below 2 mΩ cm<sup>2</sup> at 150 N cm<sup>-2</sup>, fulfilling the 10 mΩ cm<sup>2</sup> criteria from the U.S. Department of Energy.

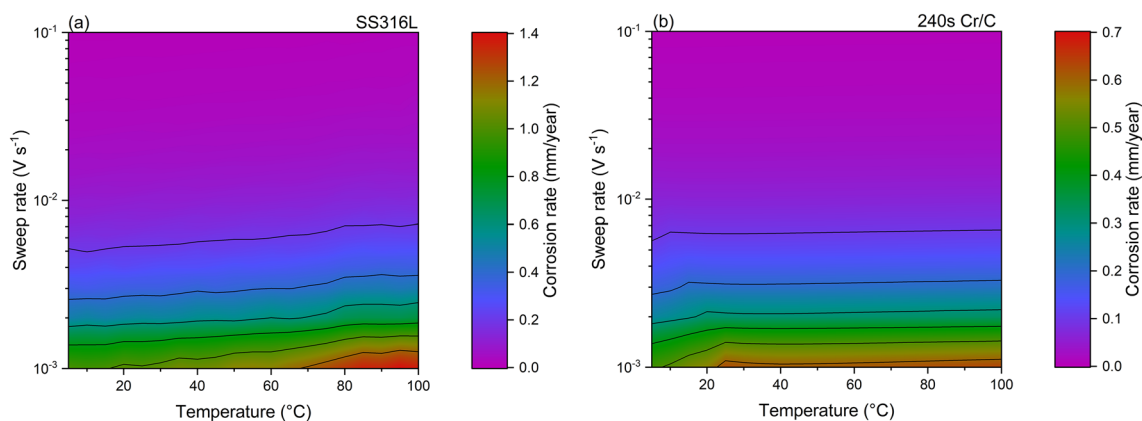


**Fig. 7** Simulated corrosion rates in mm/year as a function of temperature and potential sweep rate for **a** SS316L and **b** 240 s Cr/C-coated sample in 0.5 M H<sub>2</sub>SO<sub>4</sub>. Please note the different colour scales in both figures

- The polarisation curves revealed that the deposition of a carbon top layer leads to a 10-fold reduction of the current density ( $j = 8.22 \times 10^{-8} \text{ A cm}^{-2}$ ). At 80 °C, increased current densities were observed but the thicker Cr/C coating exhibits still the best corrosion resistance.
- Simulation results are in good agreement with experimental observations for the dissolution of chromium, nickel and iron in the CV measurements. For the bare SS316L substrate, the governing reaction can be attributed to the corrosion of chromium and nickel at the sample surface, whilst a reversible signal which corresponds to the redox equilibrium of dissolved iron ( $\text{Fe}^{2+}/\text{Fe}^{3+}$ ) can be observed for the Cr/C-coated samples.
- The dependency of the corrosion rate with temperature and potential sweep rate reveals that the fastest corrosion occurs at slow potential changes, which are typical conditions for a PEMFC setup. Modelling predictions show a reduction of the corrosion rate by a factor of two, when a Cr/C coating is applied.

Results prove that the functionality and lifetime of metallic bipolar plates for fuel cells can be improved by the multi-layer coating. In combination with the presented model, a better understanding of the governing corrosion reactions can be achieved, supporting the further development of fuel cells.

**Author contributions** MS contributed towards sample preparation, characterisation/investigation, data curation, and writing; MA contributed towards modelling, data curation, and writing; TR contributed towards supervision and writing (internal review); and CL contributed towards supervision and writing (internal review)

**Funding** Open Access funding enabled and organized by Projekt DEAL.

## Declarations

**Conflict of interest** The authors declare no conflict of interest.

**Open Access** This article is licensed under a Creative Commons Attribution 4.0 International License, which permits use, sharing, adaptation, distribution and reproduction in any medium or format, as long as you give appropriate credit to the original author(s) and the source, provide a link to the Creative Commons licence, and indicate if changes were made. The images or other third party material in this article are included in the article's Creative Commons licence, unless indicated otherwise in a credit line to the material. If material is not included in the article's Creative Commons licence and your intended use is not permitted by statutory regulation or exceeds the permitted use, you will need to obtain permission directly from the copyright holder. To view a copy of this licence, visit <http://creativecommons.org/licenses/by/4.0/>.

## References

1. IEA (2020) Global energy review 2019. Tech. Rep., International Energy Agency, Paris. <https://www.iea.org/reports/global-energy-review-2019>. Accessed 1 June 2022
2. IEA (2020) World energy outlook 2020. Tech. Rep., International Energy Agency, Paris. <https://www.iea.org/reports/world-energy-outlook-2020>. Accessed 1 June 2022
3. Gaedicke C et al (2020) BGR energy study 2019. data and developments concerning german and global energy supplies. Tech. Rep., Federal Institute for Geosciences and natural Resources, Hannover. [https://www.bgr.bund.de/EN/Themen/Energie/Downloads/energiestudie\\_2019\\_en.pdf](https://www.bgr.bund.de/EN/Themen/Energie/Downloads/energiestudie_2019_en.pdf). Accessed 1 June 2022
4. Carrette L, Friedrich K, Stimming U (2000) Fuel cells: principles, types, fuels, and applications. *ChemPhysChem Eur J Chem Phys Phys Chem* 1:162–193. [https://doi.org/10.1002/1439-7641\(20001215\)1:4162::AID-CPHC1623.0.CO;2-Z](https://doi.org/10.1002/1439-7641(20001215)1:4162::AID-CPHC1623.0.CO;2-Z)
5. Gröger O, Gasteiger H, Suchsland J (2015) Review-electromobility: batteries or fuel cells? *J Electrochem Soc* 162:2605–2622. <https://doi.org/10.1149/2.0211514jes>
6. Davies D, Adcock P, Turpin M, Rowen S (2000) Stainless steel as a bipolar plate material for solid polymer fuel cells. *J Power Sourc* 86:237–242. [https://doi.org/10.1016/S0378-7753\(99\)00524-8](https://doi.org/10.1016/S0378-7753(99)00524-8)
7. Wang H, Sweikart M, Turner J (2003) Stainless steel as bipolar plate material for polymer electrolyte membrane fuel cells. *J Power Sourc* 115:243–251. [https://doi.org/10.1016/S0378-7753\(03\)00023-5](https://doi.org/10.1016/S0378-7753(03)00023-5)
8. Tawfik H, Hung Y, Mahajan D (2007) Metal bipolar plates for PEM fuel cell—a review. *J Power Sourc* 163:755–767. <https://doi.org/10.1016/j.jpowsour.2006.09.088>
9. Xu Z, Qiu D, Yi P, Peng L, Lai X (2020) Towards mass applications: a review on the challenges and developments in metallic bipolar plates for PEMFC. *Prog Nat Sci: Mater Int* 30:815–824. <https://doi.org/10.1016/j.pnsc.2020.10.015>
10. Yoon W, Huang X, Fazzino P, Reifsnider K, Akkaoui M (2008) Evaluation of coated metallic bipolar plates for polymer electrolyte membrane fuel cells. *Int J Electrochem Sci* 179:265–273. <https://doi.org/10.1016/j.jpowsour.2007.12.034>
11. Asri N, Husaini T, Sulong A, Majlan E, Daud W (2019) Coating of stainless steel and titanium bipolar plates for anticorrosion in PEMFC: a review. *Int J Hydrog Energy* 42:9135–9148. <https://doi.org/10.1016/j.ijhydene.2016.06.241>
12. Makkus R, Janssen A, de Bruijn F, Mallant R (2000) Use of stainless steel for cost competitive bipolar plates in the SPFC. *J Power Sourc* 86:274–282. [https://doi.org/10.1016/S0378-7753\(99\)00460-7](https://doi.org/10.1016/S0378-7753(99)00460-7)
13. Mohr P (2018) *Optimierung von Brennstoffzellen-Bipolarplatten für die automobile Anwendung*. Ph.D. thesis, University Duisburg-Essen. [https://duepublico2.uni-due.de/receive/duepublico\\_mods\\_00045782](https://duepublico2.uni-due.de/receive/duepublico_mods_00045782)
14. Liang P et al (2018) Contact resistance prediction of proton exchange membrane fuel cell considering fabrication characteristics of metallic bipolar plates. *Energy Convers Manage* 169:334–344. <https://doi.org/10.1016/j.enconman.2018.05.069>
15. Cheng X et al (2007) A review of PEM hydrogen fuel cell contamination: impacts, mechanisms, and mitigation. *J Power Sourc* 165:739–756. <https://doi.org/10.1016/j.jpowsour.2006.12.012>
16. Kim J-H et al (2011) Niobium sputter coated stainless steel as a bipolar plate material for polymer electrolyte membrane fuel cell stacks. *Int J Electrochem Sci* 6:4365–4377
17. Zhang H et al (2012) CrN/Cr multilayer coating on 316l stainless steel as bipolar plates for proton exchange membrane fuel cells. *J Power Sourc* 198:176–181. <https://doi.org/10.1016/j.jpowsour.2011.09.091>
18. Huang N et al (2016) Corrosion kinetics of 316l stainless steel bipolar plate with chromiumcarbide coating in simulated PEMFC cathodic environment. *Results Phys* 6:730–736. <https://doi.org/10.1016/j.rinp.2016.10.002>
19. Wang S et al (2019) Ti/(Ti, Cr)N/CrN multilayer coated 316l stainless steel by arc ion plating as bipolar plates for proton exchange

- membrane fuel cells. *J Energy Chem* 26:168–174. <https://doi.org/10.1016/j.jechem.2016.09.004>
20. Manso A et al (2020) Corrosion behavior of tantalum coatings on AISI 316L stainless steel substrate for bipolar plates of PEM fuel cells. *Int J Hydrog Energy* 45:20679–20691. <https://doi.org/10.1016/j.ijhydene.2019.12.157>
  21. Xu M et al (2020) Properties of a plasma-nitrided coating and a CrNx coating on the stainless steel bipolar plate of PEMFC. *Coatings*. <https://doi.org/10.3390/coatings10020183>
  22. Yi P, Peng L, Feng L, Gan P, Lai X (2010) Performance of a proton exchange membrane fuel cell stack using conductive amorphous carbon-coated 304 stainless steel bipolar plates. *J Power Sourc* 195:7061–7066. <https://doi.org/10.1016/j.jpowsour.2010.05.019>
  23. Larijani M, Yari M, Afshar A, Jafarian M, Eshghabadi M (2011) A comparison of carbon coated and uncoated 316L stainless steel for using as bipolar plates in PEMFCs. *J Alloys Compd* 509:7400–7404. <https://doi.org/10.1016/j.jallcom.2011.04.044>
  24. Husby H, Kongstein O, Oedegaard A, Seland F (2014) Carbon-polymer composite coatings for PEM fuel cell bipolar plates. *Int J Hydrog Energy* 39:951–957. <https://doi.org/10.1016/j.ijhydene.2013.10.115>
  25. Mingge W et al (2016) Chromium interlayer amorphous carbon film for 304 stainless steel bipolar plate of proton exchange membrane fuel cell. *Surf Coat Technol* 307(A):374–381. <https://doi.org/10.1016/j.surfcoat.2016.07.069>
  26. Mingge W et al (2016) Effects of metal buffer layer for amorphous carbon film of 304 stainless steel bipolar plate. *Thin Solid Films* 616:507–514. <https://doi.org/10.1016/j.tsf.2016.07.043>
  27. Steinhorst M, Giorgio M, Topalski S, Roch T (2019) Investigation of carbon-based coatings on austenitic stainless steel for bipolar plates in proton exchange membrane fuel cells, produced by cathodic arc deposition. In: *Proceedings of the FC<sup>3</sup> - 1st Fuel Cell Conference Chemnitz 2019 - Saubere Antriebe. Effizient Produziert.*, pp 1–8. <https://nbn-resolving.org/urn:nbn:de:bsz:chl-qucos-a2-361973>. ISBN 978-3-96100-103-3
  28. Hu R, Tang J, Zhu G, Deng Q, Lu J (2019) The effect of duty cycle and bias voltage for graphite-like carbon film coated 304 stainless steel as metallic bipolar plate. *J Alloys Compd* 772:1067–1078. <https://doi.org/10.1016/j.jallcom.2018.09.169>
  29. Alaefour I, Shahgaldi S, Zhao J, Li X (2021) Synthesis and ex-situ characterizations of diamond-like carbon coatings for metallic bipolar plates in PEM fuel cells. *Int J Hydrog Energy* 46:11059–11070. <https://doi.org/10.1016/j.ijhydene.2020.09.259>
  30. Yi P, Zhang D, Qiu D, Peng L, Lai X (2019) Carbon-based coatings for metallic bipolar plates used in proton exchange membrane fuel cells. *Int J Hydrog Energy* 44:6813–6843. <https://doi.org/10.1016/j.ijhydene.2019.01.176>
  31. Miyazawa A, Tada E, Nishikata A (2013) Influence of corrosion of SS316L bipolar plate on PEFC performance. *J Power Sourc* 231:226–233. <https://doi.org/10.1016/j.jpowsour.2012.12.088>
  32. Papadias D et al (2015) Degradation of SS316L bipolar plates in simulated fuel cell environment: corrosion rate, barrier film formation kinetics and contact resistance. *J Power Sourc* 273:1237–1249. <https://doi.org/10.1016/j.jpowsour.2014.02.053>
  33. Wanklyn J (1981) The role of molybdenum in the crevice corrosion of stainless steels. *Corros Sci* 21:211–225. [https://doi.org/10.1016/0010-938X\(81\)90031-7](https://doi.org/10.1016/0010-938X(81)90031-7)
  34. Ha H, Lee T, Bae J, Chun D (2018) Molybdenum effects on pitting corrosion resistance of FeCrMnMoNC austenitic stainless steels. *Metals* 8(653):1–13. <https://doi.org/10.3390/met8080653>
  35. Szweczyk-Nykiel A (2015) The influence of molybdenum on corrosion resistance of sintered austenitic stainless steel. *Tech Trans Mech* 4:1–12. <https://doi.org/10.4467/2353737XCT.15.344.4865>
  36. Outokumpu. *Supra* 316L/4404 (2020). [https://secure.outokumpu.com/steelfinder/properties/GradeDetail.aspx?OTKBrandNameID=00602\\_&Category=Supra\\_&\\_gl=1\\*112fdos\\*\\_up\\*MQ..&gclid=EAIAIQobChMIo-ux6LSy\\_AIVj9Z3Ch3rAqskEAAAYSAAEgLT5vD\\_BwE](https://secure.outokumpu.com/steelfinder/properties/GradeDetail.aspx?OTKBrandNameID=00602_&Category=Supra_&_gl=1*112fdos*_up*MQ..&gclid=EAIAIQobChMIo-ux6LSy_AIVj9Z3Ch3rAqskEAAAYSAAEgLT5vD_BwE). Accessed 06 Jan 2023
  37. Hamann C, Hamnett A, Vielstich W (2007) *Electrochemistry*, 2nd edn. Wiley, Weinheim
  38. Auinger M et al (2011) Near-surface ion distribution and buffer effects during electrochemical reactions. *Phys. Chem. Chem. Phys.* 13:16384–16394. <https://doi.org/10.1039/c1cp21717h>
  39. Lechner M (2007) Landolt Börnstein—numerical data and functional relationships in science and technology, group VI: physical chemistry, vol 9A. Springer, Berlin
  40. Dafft E, Bohnenkamp K, Engell H (1979) Investigations of the hydrogen evolution kinetics and hydrogen absorption by iron electrodes during cathodic polarization. *Corros Sci* 19:591–612
  41. Atkins P, de Paula J (2006) *Physical chemistry*, 8th edn. W.H. Freeman and Company, New York
  42. Anson F (1961) Exchange current densities for Fe(II)-Fe(III) solutions in sulfuric acid and perchloric acid. *Anal Chem* 33:939–942
  43. Hydrogen and Fuel Cell Technologies Office (2017) Hydrogen and fuel cell technologies office multi-year research, development, and demonstration plan. Tech. Rep., U.S. Department of Energy, Washington D.C. [https://www.energy.gov/sites/default/files/2017/05/f34/fcto\\_myrrdd\\_fuel\\_cells.pdf](https://www.energy.gov/sites/default/files/2017/05/f34/fcto_myrrdd_fuel_cells.pdf). Accessed 6 Jan 2023
  44. Bojinov M, Fabricius G, Laitinen T, Saario T (1998) The mechanism of the transpassive dissolution of chromium in acidic sulfate solutions. *J Electrochem Soc* 145:2043–2050. <https://doi.org/10.1149/1.1838595>
  45. Quang K, Traisnel M, Damie P (1980) Influence of chemical composition and temperature on the passivation of some stainless steels and nickel-based alloys in sulphuric acid. *J Appl Electrochem* 70:703–708. <https://doi.org/10.1007/BF00611273>
  46. Bellezze T, Giuliani G, Roventi G (2018) Study of stainless steels corrosion in a strong acid mixture. part 1: cyclic potentiodynamic polarization curves examined by means of an analytical method. *Corros Sci* 130:113–125. <https://doi.org/10.1016/j.corsci.2017.10.012>
  47. Panjan P, Drnovšek A, Gselman P, Cekada M, Panjan M (2020) Review of growth defects in thin films prepared by PVD techniques. *Coatings*. <https://doi.org/10.3390/coatings10050447>
  48. Liu G et al (2010) RDE measurements of ORR activity of Pt<sub>1-x</sub>Ir<sub>x</sub> (0 < x < 0.3) on high surface area NSTF-coated glassy carbon disks. *J Electrochem Soc* 157:B207–B214. <https://doi.org/10.1149/1.3262522>



## Authors and Affiliations

Maximilian Steinhorst<sup>1,2</sup>  · Michael Auinger<sup>3,4</sup> · Teja Roch<sup>1</sup> · Christoph Leyens<sup>1,2</sup>

✉ Maximilian Steinhorst  
maximilian.steinhorst@iws.fraunhofer.de

✉ Michael Auinger  
michael.auinger.at@ieee.org

<sup>1</sup> Fraunhofer Institute for Material and Beam Technology IWS,  
Winterbergstraße 28, 01277 Dresden, Saxony, Germany

<sup>2</sup> Institute of Material Science, Technische Universität  
Dresden, Helmholtzstraße 7, 01069 Dresden, Saxony,  
Germany

<sup>3</sup> WMG, University of Warwick, 6 Lord Bhattacharyya Way,  
Coventry CV4 7AL, West Midlands, UK

<sup>4</sup> Institute of Chemical Technologies and Analytics, TU Wien,  
Getreidemarkt 9, Vienna 1060, Vienna, Austria